Mon. Not. R. Astron. Soc. **000**, 000–000 (0000) Printed 2 February 2008 (MN LATEX style file v2.2)

Ten eclipsing binaries in the Small Magellanic Cloud: fundamental parameters and SMC distance

Tim J. Harries[1], Ron W. Hilditch[2], and Ian D. Howarth[3]
[1] *School of Physics, University of Exeter, Stocker Road, Exeter EX4 4QL, England.*
[2] *School of Physics and Astronomy, University of St. Andrews, North Haugh, St. Andrews, Fife KY16 9SS, Scotland.*
[3] *Department of Physics and Astronomy, University College London, Gower Street, London WC1E 6BT, England.*

arXiv:astro-ph/0210295v1 14 Oct 2002

Dates to be inserted

ABSTRACT
We present the first results of an observational programme to measure the fundamental parameters of over 100 eclipsing binaries in the Small Magellanic Cloud (SMC). The spectroscopic data were obtained by using the 2dF multi-object spectrograph on the 3.9-m Anglo-Australian Telescope, and are used in conjunction with photometry from the OGLE database of SMC eclipsing binaries. Ten systems are discussed in this first paper. Three are detached early-B binaries, six are in a semi-detached configuration, and one is in a marginal contact state. We conclude that the semi-detached systems are undergoing the slow mass-transfer phase of case-A binary evolution, in which the mass donor has reached its Roche lobe while still on the main sequence. Each system provides a primary distance indicator. By constructing a new calibration between spectral type and temperature for O and early B stars, we find a mean distance modulus to the SMC of 18.89 ± 0.04 (statistical) ± 0.10 (systematic). This value represents one of the most precise determinations to date of the distance to the SMC.

Key words: Stars - binaries; Galaxies - individual - Small Magellanic Cloud

1 INTRODUCTION

The extragalactic distance scale is based on a small number of calibrators, with Cepheids being the most widely adopted, primarily due to the relative ease with which these objects may be identified and measured in distant galaxies. However, other distance indicators, such as red-clump and RR Lyrae stars, retain a critically important rôle in verifying the Cepheid distance scale. Eclipsing, double-lined spectroscopic binaries (eSB2s) not only provide a direct route to fundamental determinations of stellar masses and radii, but also afford true *primary* distance indicators if temperatures (more precisely, surface fluxes) can be assigned to the components. Our experience with studies of Galactic early-type binaries has shown us that, with care, distance moduli accurate to ± 0.1 mag are attainable (Hilditch, Harries & Bell 1996; Harries, Hilditch & Hill 1997; Harries, Hilditch & Hill 1998), a precision comparable to that obtained for individual Cepheid variables.

Distance determinations for eSB2s require densely sampled photometric and spectroscopic data; such determinations have, therefore, traditionally been observationally demanding, typically requiring several nights of 4-m-class telescope time per object. Two recent developments have allowed significant advances in this area as far as the Magellanic Clouds are concerned. First, one of the valuable legacies of the various microlensing surveys is a vast database of newly discovered eclipsing binaries, with well-defined ephemerides and well-sampled, high-quality, multi-colour photometry; the OGLE survey alone has yielded over 1400 new eclipsing binaries in the Small Magellanic Cloud (SMC; Udalski et al. 1998b). Secondly, multi-object fibre-fed spectrographs now allow data to be collected for many objects simultaneously. In this paper we report the first results of a programme intended to determine fundamental parameters of $\sim$100 massive binaries in the SMC, by combining OGLE photometry with spectroscopy obtained by using the 2dF multi-object spectrograph on the Anglo-Australian Telescope (AAT).

The Magellanic Clouds constitute a crucial rung in the 'distance ladder', but recent determinations of their distance moduli (DMi) have split between 'short' and 'long' scales (DMi $\sim$18.3 and $\sim$18.5 for the LMC; e.g., Cole 1998). The earliest attempt to derive a DM for an individual eSB2 in the SMC was by Howarth (1982), who found a DM of 18.3 for the X-ray binary Sk 160, located in the wing of the SMC ($\sim$0.3 mag closer than the main body of the SMC according to Caldwell & Coulson 1986). Bell et al. (1991) presented the first eSB2-based DM for the SMC itself, using HV 2226 to estimate a DM of 18.6 ± 0.3. Guinan and coworkers are currently undertaking a programme to study

in detail individual B-star binaries in the LMC, using HST spectra to determine temperatures and reddenings simultaneously. To date, this work has led to distances to two objects, HV 2274 (Guinan et al. 1998; Ribas et al. 2000) and HV 982 (Fitzpatrick et al. 2002). The DM found for HV 2274 (18.35 ± 0.07) appears to support the short distance scale to the Clouds, but the DM of HV 982 found by Fitzpatrick et al. (2002; 18.50) is consistent with the long distance scale. Re-analysis of the HV 2274 data by other authors has also resulted in larger DM estimates (18.40 ± 0.07, Nelson et al. 2000; 18.46 ± 0.06, Groenewegen & Salaris 2001).

The aims of our programme are to provide a reliable eSB2-based distance estimate for the SMC, and to determine masses, radii and temperatures for ∼200 stars. These data will be used to test low-metallicity stellar-evolution models for both single stars (the detached systems) and interacting binary systems (the semi-detached and contact objects). The present paper is a first step in this direction. We summarize the selection criteria for the sample, and the spectroscopic observations, in Section 2. We then describe the basic steps in the analysis, and tabulate our results for the first ten programme objects. Finally, we report our initial distance estimate, and compare our result with work based on red-clump stars and the Cepheid period–luminosity relation.

2 OBSERVATIONS

We base our sample on the OGLE database of SMC eclipsing binaries (Udalski et al. 1998). The SMC stellar population is of intrinsic interest as the most easily observed sample of low-metallicity objects, and the quality of the OGLE photometry and astrometry is well suited to our project. To define the target sample, two filters were initially applied to the OGLE eclipsing-binary database: $B < 16$, to allow sufficient signal-to-noise on our faintest targets (S:N $\gtrsim 25$ per wavelength sample); and orbital period $P_{\rm orb} < 5$d, to ensure adequate phase coverage for most targets in our first 5-night allocation of observing time.

Our spectroscopy was obtained with the 2dF instrument, which is capable of securing up to 400 spectra simultaneously, using 200 fibre feeds to each of two spectrographs (Lewis et al. 2002). It has a 2° field of view, and two substantially overlapping fields were therefore required to ensure complete coverage of the 2.5 square degree OGLE region. The adopted field centres were $00^{\rm h}\,47^{\rm m}\,00^{\rm s}\ -73^\circ\,10'00''$ (J2000, herein Field 1), and $01^{\rm h}\,00^{\rm m}\,00^{\rm s}\ -72^\circ\,45'\,00''$ (Field 2). Astrometry accurate to better than $0.5''$ is essential for 2dF observations, since the fibre diameter is only $2''$. We cross-correlated the OGLE catalogue against SuperCosmos source lists and found good agreement in relative position, with a sub-arcsecond offset in right ascension and declination. We therefore used the OGLE positions to assign the 2dF fibre positions. Fibre-allocation constraints (such as fibre crossings and angular proximity of targets) meant that a few stars in the filtered catalogue were unobservable. The final target list consists of 124 binaries, of which 69 were in the overlap region of the two fields.

Digitized Sky Survey (DSS) images were examined to identify sky regions in these densely populated fields, and the sky positions manually allocated. Bright ($14 < V < 15$) fiducial, or guide, stars were selected from the full OGLE catalogue, and DSS images of the objects were again inspected to ensure that there were no blended or other close companions.

The data were obtained in service mode by T. Bridges during the nights of 2001 Sept. 6–11 (JDs 2,452,158–63), with one test exposure of Field 1 taken on Sept. 5; the night of Sept. 7 was lost to cloud. Integration times of 1800s were used for most target exposures, in seeing of typically 1.5–2 arcseconds. As each field contained fewer than 200 targets, only the better-performing of the 2dF spectrographs was employed. A 1200B grating was used, providing a mean reciprocal dispersion of $1.1\text{Å}\,\text{px}^{-1}$, and a resolution of 2 Å ($135\ \text{km}\,\text{s}^{-1}$). The wavelength range of the data is 3855Å to 4910Å, a region which contains spectral lines suitable for both radial-velocity measurements and spectral typing in the classification regime of interest.

Arc and flatfield frames were obtained after each target exposure, along with offset sky frames (which may be used to calibrate fibre throughput), and twilight-sky integrations. The 2dFdr package was used to reduce the data, with default settings (Lewis et al. 2002). Twilight-sky observations were used to calibrate the system throughputs when possible. The final dataset comprises 32 exposures (16 per field), so each system has at least 16 orbital-phase points, with rather more than half the targets having 32 phase points.

For the present study we selected ten binaries on the basis of spectral signal-to-noise and coverage of quadrature phases (the times of maximum radial-velocity separation, best constraining the orbital velocity amplitudes). The selected objects are listed in Table 1, and examples of typical spectra are shown in Figure 1.

3 DATA ANALYSIS

The spectra were first normalized by using low-order polynomial fits to interactively defined line-free continuum regions, and were then velocity-corrected to the heliocentric frame. Throughout, we assumed circular orbits for all our objects, since their orbital periods are short, the sizes of the stars relative to their separation prove to be large ($r/a > 0.25$), and all the light curves have secondary minima at orbital phase 0.5.

3.1 Component spectra and orbital parameters

We used two independent methods to obtain the velocity semi-amplitudes and to separate the component spectra. The first was the disentangling algorithm of Simon & Sturm (1994), in which an over-determined matrix equation is constructed from the data and a *given* orbital solution, and is solved by using singular-value decomposition (SVD). We obtained the best-fitting orbital solution by minimization of the SVD residuals (by using a grid search followed by a downhill simplex).

The second method involves fitting for the two component spectra by using a constrained non-linear least-squares algorithm (Byrd et al. 1995), again for a given set of orbital parameters. A genetic algorithm (Charbonneau & Knapp 1995) was used to search for the orbital parameters which yielded the minimum in χ^2 hyperspace.

Both methods assume that the component spectra do

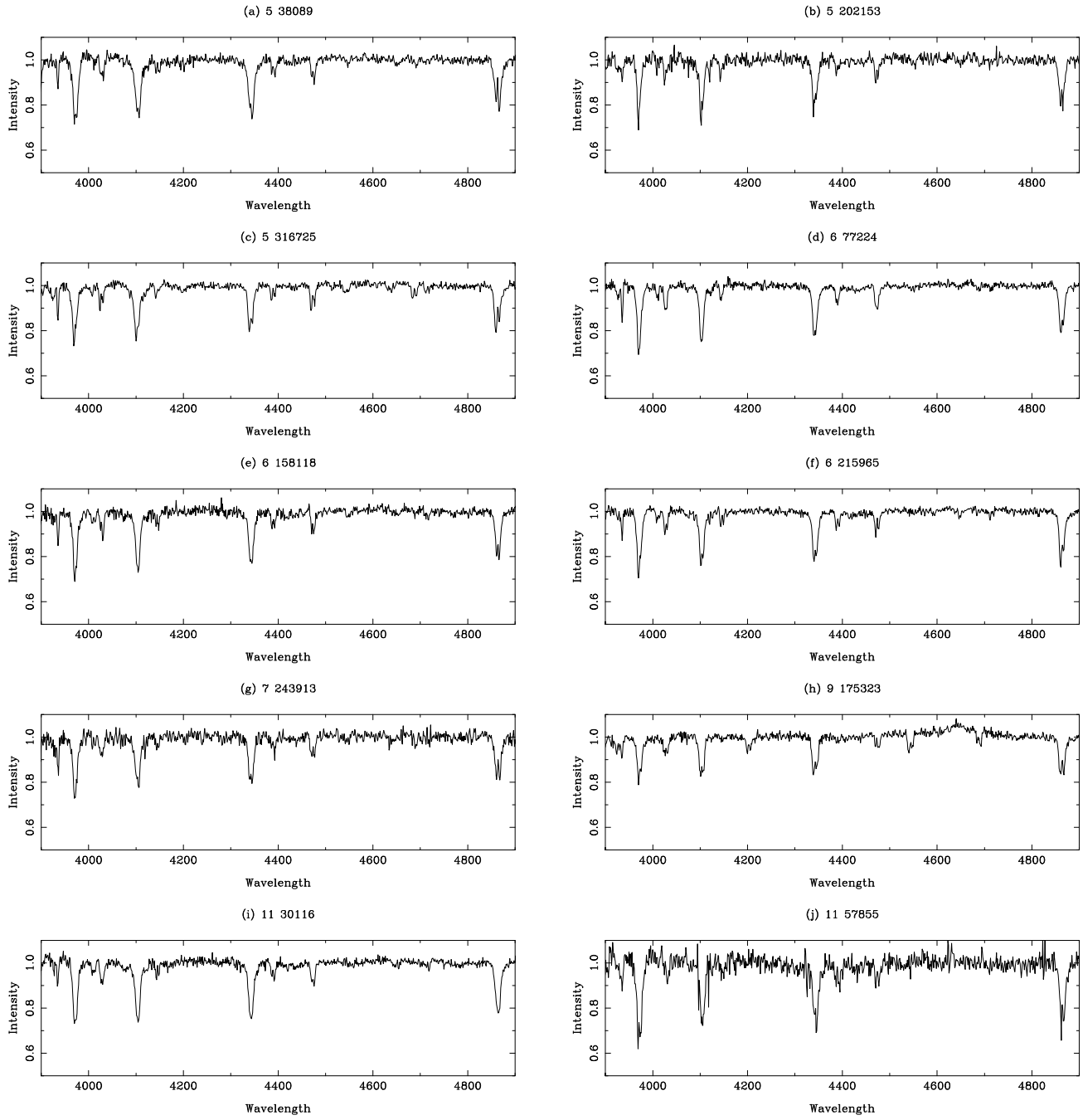

Figure 1. Illustrative spectra of the targets discussed in this paper, taken close to maximum postive velocity of the primary (spectroscopic phase zero, photometric phase 0.75). The strong absorption lines visible include Hδ, Hγ, Hβ, He I λ4471. Note that in several cases (e.g., 9 175323) the absorption lines of both components are clearly visible.

not change with orbital phase. Though not strictly correct (because of the aspect-dependent effects of gravity darkening and 'reflection'), this is a good approximation, except during eclipses, when the apparent intensity ratios of the components change significantly. Spectra obtained during eclipses were therefore excluded from the analyses. This entails no loss of leverage on the determination of the velocity semi-amplitudes, which are constrained by spectra obtained at quadratures, but does mean that the time of maximum positive velocity of the primary is less well-constrained. We therefore fixed the spectroscopic phases using the OGLE ephemerides.

We found good agreement between the two RV analysis methods. In practice we adopted the least-squares technique (which is computationally faster) to disentangle the spectra after the orbital parameters had been determined using the Simon & Sturm approach.

The systems considered here may have significant tidal distortions, in which case the centre of *light* (specifically, the weighted mean line velocity) will not follow the cen-

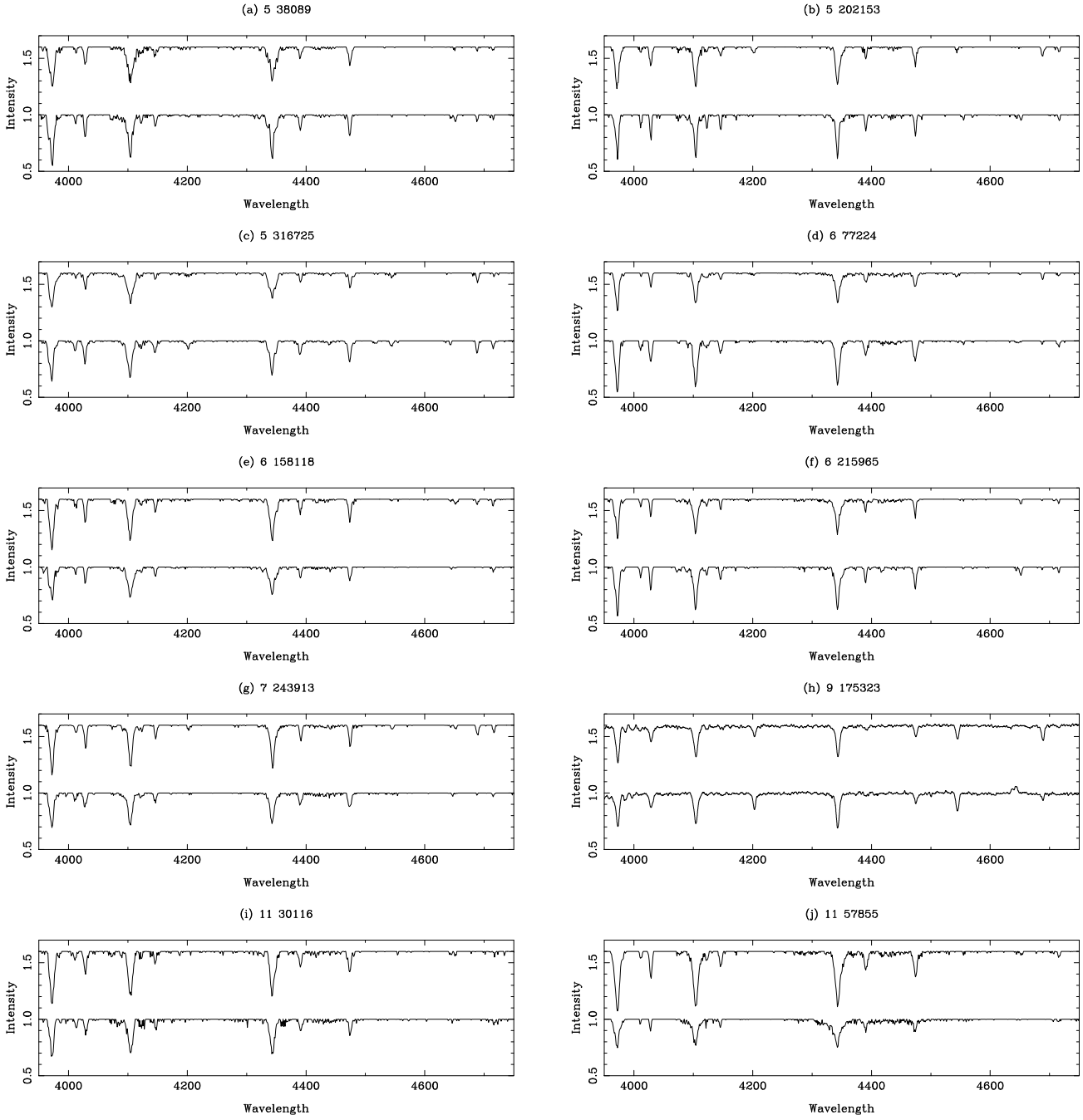

Figure 2. Component spectra for the subsample. The normalized spectra are plotted as relative intensity, with the primary offset by +0.6 for clarity. The strong absorption lines include Hϵ, Hδ, Hγ, and Hβ, and He I $\lambda\lambda$ 4026, 4144, 4388, 4471Å.

tre of *mass* (see e.g., Kopal 1959, Hilditch 2001 for descriptions and bibliographic references). We used the light-curve solutions (Section 3.3) to determine these so-called 'non-Keplerian' corrections, and applied them to the derived velocity semi-amplitudes. We found that a single iteration between the light-curve and radial-velocity solutions achieved convergence in these corrections, which are typically on the order of $5\,\mathrm{km\,s^{-1}}$ (and always less than $10\,\mathrm{km\,s^{-1}}$). The final values for the velocity semi-amplitudes for the primary[1] and secondary components (K_1 and K_2) are listed in Table 2, together with the formal uncertainties from the solutions. Further details of individual solutions are included in Section 3.4.

Of course, the separated spectra of the binary compo-

[1] We use the convention that the primary is the star eclipsed at primary (i.e., deeper) eclipse; it has the higher surface brightness, but is not necessarily the more massive component.

Table 1. Basic parameters for the targets studied here. Columns list the stars OGLE identification (the first figure refers to the OGLE field, the second the star number within that field); the co-ordinates; photometric period; and OGLE I magnitude and colours outside eclipse (the I magnitudes are quadrature values, returned from the normalization of the light-curve analysis described in Section 3.3).

Star Number	α (J2000) h m s	δ (J2000) $^\circ$ $'$ $''$	$P_{\rm orb}$ d	I	$B-V$	$V-I$
5 038089	00 49 01.85	−73 06 06.9	2.38946	15.228	−0.222	−0.144
5 202153	00 50 27.93	−73 03 16.1	4.60677	14.265	−0.215	−0.150
5 316725	00 51 05.95	−72 40 56.7	2.55606	14.691	−0.257	−0.142
6 077224	00 51 50.13	−72 39 22.7	3.82087	14.009	−0.128	−0.148
6 158118	00 52 19.28	−72 41 51.7	2.57832	15.057	−0.085	−0.156
6 215965	00 53 33.35	−72 56 24.1	3.94604	14.123	−0.204	−0.209
7 243913	00 56 56.34	−72 49 06.4	2.63160	14.859	−0.150	−0.096
9 175323	01 03 21.27	−72 05 37.8	2.20596	13.675	−0.232	−0.181
11 30116	01 06 24.86	−72 12 48.3	2.95427	14.878	−0.200	−0.167
11 57855	01 07 31.44	−72 19 52.9	1.29695	16.000	−0.248	−0.201

nents have arbitrary normalizations: there is complete redundancy between line strengths and relative continuum levels (i.e., it is, in principle, impossible to distinguish between a relatively faint secondary with intrinsically strong absorption lines, and a relatively bright secondary with intrinsically weak absorption lines). However, by requiring the line strengths in the spectra of the two components to be in the expected ratio, it is possible to obtain a spectroscopic estimate of their relative ($\sim B$-band) continuum fluxes.

Systemic velocities for the primary and secondary components were determined by cross-correlating the disentangled spectra with that of the O9 star 10 Lac (HD 214680) which has a heliocentric radial velocity of $-9\,{\rm km\,s^{-1}}$(Holmgren, Hill & Fisher 1990). The cross-correlation function was fitted, by least squares, with a Gaussian. We found that the systemic velocities of the components in a given binary agreed to within their associated formal errors, and we quote the mean systemic velocity for each system in Table 2. The velocities, which range from 164 to 211 ${\rm km\,s^{-1}}$, are consistent with the targets' location according to the radial-velocity maps given by Mathewson, Ford & Visvanathan (1988).

Finally, it should be noted that the orbital parameters are determined directly from the ensemble of spectra of a given target, with no intermediate explicit radial-velocity measurements. However, for the convenience of future researchers, we have, *as a separate exercise*, measured the stellar radial velocities, by least-squares fitting the disentangled component spectra to the observed spectra; results are given in Appendix A. Although traditional circular-orbit spectroscopic solutions of these measured velocities yield semi-amplitudes that agree, within the errors, with those listed in Table 2, the latter – which include small non-Keplerian corrections – offer the best representations of the orbital characteristics available at present.

3.2 Spectroscopic classification

The separate component spectra of all the stars were classified by reference to the digital atlas of galactic OB stars by Walborn & Fitzpatrick (1990) and the study of SMC B supergiants by Lennon (1997). (The lack of absolute normalizations for the component spectra is of no consequence for spectroscopic classifications, which depend only on relative line strengths.) This task was performed independently by all three authors in order to quantify the uncertainities associated with the spectral types. Typically, we found that our classifications agreed to within one temperature type. (We did not generally classify the luminosity class, since the traditional indicators include metal lines, which are of course much weaker in the SMC compared to the Galactic templates.) The adopted spectral types, which represent the mode of the three individual estimates, are included in Table 3.

3.3 Light-curve analysis

It is well known that light curves with alternating total and annular eclipses (complete eclipses) provide the best determinations of the photometric elements. Photometric determinations of the mass-ratio (q) can approach the accuracy of determinations from independent spectroscopic data (radial velocity curves of both components) but only in such favoured cases.

In this particular sample of 10 binaries, selected principally by the number and quality of spectra secured around both quadratures, 9 out of 10 systems display only *partial* eclipses. Only 5 202153 has total/annular eclipses but its light curve has notable asymmetries as noted below. Accordingly, the possible separation of the dependence of light-curve shape upon inclination (i) and mass ratio (q) is denied, and it is again well established that a light curve may be fitted equally well by a range of pairs of values (i, q) that can be substantial, dependent primarily upon the degree of distortion of both stars.

For these reasons we adopted a pragmatic procedure of solving each light curve with the mass ratio fixed at the value determined spectroscopically. This breaks the degeneracy between i and q and in our experience yields better results than any grid search for a minimum χ^2 in (i, q) space from the photometry alone. For most systems, this procedure of adopting the spectroscopic q has enabled I-band light-curve solutions to be found readily that also reproduce the flux ratio observed spectroscopically in the B-band. In a few cases, noted below, it proved necessary to constrain the solution further by using the spectroscopic B-band flux ratio to fix either the secondary temperature or secondary radius.

In summary, we have used all the observational data available to us to establish the set of parameters that matches best all of the data. In a few cases, the light-curve solution is slightly poorer than would be determined by concentrating on the light curve alone, but such light-curve solutions do not agree with other parts of the available data. It should further be noted that by undertaking an analysis of a large sample, problems with individual systems, and uncertainties resulting from partial eclipses, are both diluted, and should average out.

Fits were made to the Cousins I-band OGLE photometry of the targets, using Hill's LIGHT2 code (Hill 1979; Hill & Rucinski 1993). The light-curve analysis yields, essentially, the surface-brightness ratio of the components, although it offers no *direct* information on the actual stellar temperatures. We therefore fixed the primary's temperature using a spectral-type–temperature calibration (see Section 6.1). The mass ratio was also fixed, from the radial-velocity solution, and the photometry was then usually solved for the primary and secondary radii, the orbital inclination, and the secondary temperature (which follows from the surface-brightness ratio). Where preliminary solutions indicated Roche-lobe-filling components, the corresponding radii were subsequently constrained accordingly. Results are given in Table 3; model fits are compared to the data in Figure 3; and details of individual fits follow. In all cases, we assumed synchronous rotation (in the absence of evidence to the contrary), limb-darkening coefficients appropriate to the local temperatures, and gravity-darkening and 'reflection' coefficients appropriate to ionized radiative envelopes.

We quote "surface area" radii, viz

$$R^2 = \frac{1}{4\pi}\int dA \tag{1}$$

and mean temperatures;

$$T^4_{\rm mean} = L/4\pi\sigma R^2 \tag{2}$$

where

$$L = \sigma \int T^4 dA \tag{3}$$

and σ is the Stefan-Boltzmann constant. We note that the differences between the "mean area" radius and the oft-quoted "mean volume" radius are generally rather small (smaller in fact that the errors on the radii). The errors quoted are taken from the covariance matrix of the light-curve solution, and are formally propagated through to the final system parameters.

Udalski et al. (1998b) make no explicit statement about the accuracy of their light-curve ephemerides. We found it necessary to allow for shifts in orbital phase of an entire light curve relative to a theoretical model fit in order to minimize the χ^2 value. The largest phase shift was +0.0100 for the system 6 77224, with the remainder all less than ±0.0060, and some being zero. The average phase shift for the set of 10 systems was $+0.0015 \pm 0.0046$. For completeness, these ephemeris revisions were incorporated in the disentangling procedures described in Section 3.

Table 2. Radial-velocity solutions. Listed are the OGLE designation, the velocity semi-amplitudes of the primary and secondary stars (K_1 and K_2 respectively), and the systemic velocity, V_0.

Star Number	K_1 (km s^{-1})	K_2 (km s^{-1})	V_0 (km s^{-1})
5 038089	271 ± 10	242 ± 10	189 ± 8
5 202153	157 ± 8	250 ± 4	172 ± 5
5 316725	154 ± 11	295 ± 9	169 ± 9
6 077224	165 ± 9	201 ± 4	178 ± 5
6 158118	138 ± 5	280 ± 4	188 ± 8
6 215965	217 ± 5	202 ± 2	164 ± 6
7 243913	164 ± 8	290 ± 6	197 ± 4
9 175323	193 ± 9	280 ± 7	211 ± 3
11 30116	144 ± 21	269 ± 10	201 ± 4
11 57855	194 ± 16	293 ± 8	168 ± 9

3.4 Notes on individual targets

3.4.1 5 038089

This target was in the overlap region of the 2dF fields. Of the 32 spectra (typical S:N of 40 per pixel), 13 were within ±0.1 in orbital phase of the quadratures. Both components are clearly visible in the spectra. The flux ratio in the blue, as estimated from the component spectra, is close to unity.

The I-band light curve shows 0.3-mag-deep eclipses, of approximately equal depth, while ellipsoidal variation is evident between eclipses, indicating significant tidal distortions (Figure 3a). A detached configuration was found for this system. The solution predicts nearly-equal blue-region fluxes, which is consistent with the spectroscopy. The (O-C) curve is flat through all orbital phases demonstrating a very good fit to the light curve.

3.4.2 5 202153

This star is one of brightest considered here, and the quality of its spectra (S:N ∼50) reflects this. Fifteen spectra were used in the disentangling procedure, but the second quadrature is less well covered than the first. The primary spectrum shows strong He II absorption, which is undetected in the secondary spectrum.

We found that the light-curve solution rapidly converged to a configuration in which the secondary fills its Roche lobe. We therefore modeled the light-curve with a semi-detached configuration, solving for the secondary temperature, the primary radius, and the inclination. The solution indicates stars of roughly equal luminosity in B (which is consistent with the relative strengths of the lines in the disentangled spectra).

The I-band light curve for this star is clearly asymmetric, with the maximum at first quadrature being 0.03m brighter than that at second quadrature. Additionally, just before ingress into primary eclipse (around orbital phase 0.9) the observed curve is lower by up to 0.06m than the corresponding egress phases around phase 0.1. These asymmetries are clearly seen in Fig. 3b which compares the observations with the best-fit model light curve that is mirror-symmetric about phase 0.5. The asymmetry around ingress is suggestive of attenuation by an accretion stream from the

Roche-lobe filling secondary falling towards the primary, but the explanation for the higher maximum at first quadrature is unclear. It is difficult to quantify how much these asymmetries in the I-band light curve affect the determination of the system parameters and its distance modulus.

3.4.3 5 316725

Our spectra typically have S:N ratios of 30–40. The quadrature phases are well-sampled, with 6 observations at first quadrature and 8 at second. The secondary's spectral features appear to be stronger than those of the primary.

The I-band light curve shows relatively deep eclipses of comparable depth ($\sim$ 0.4 mag), with significant ellipsoidal variations. We found that the solution consistently converged to a semi-detached configuration, and we therefore solved for the primary radius, the secondary temperature and the inclination, with the secondary filling its Roche lobe. The solution gives a B-band flux ratio (p/s) of 0.7–0.8 around the quadratures, which is consistent with the relative line strengths in the disentangled spectra. The (O-C) curve is flat through all orbital phases demonstrating a very good fit to the light curve.

3.4.4 6 077224

The spectra of this binary typically have a S:N of $\gtrsim$50, and quadrature phases are well sampled (11 at first, 9 at second). The primary's spectrum shows He II features that are undetectable in the secondary, whose absorption lines appear otherwise to be stronger than the primary, indicating an inverted light ratio in this object.

The I-band light curve shows large ellipsoidal variation combined with shallow eclipses of approximately equal depth. A semi-detached solution gives the best fit, and we solved for the primary radius, secondary temperature, and the inclination (with the secondary star filling its Roche lobe). The light-curve solution gives a B-band flux ratio (p/s) of 0.8, in accord with the line strengths of the disentangled component spectra. The (O-C) curve is nearly flat through all orbital phases with only a small offset just before ingress to primary eclipse in this semi-detached system.

3.4.5 6 158118

This is one of the fainter objects in the sample ($V \simeq 15.1$) and the spectroscopic S:N is relatively poor (typically $\sim$30). Quadrature phases are reasonably well covered, with 3 spectra at first quadrature and 9 at second. We find that the primary's spectrum is much stronger than that of the secondary.

Although the phase coverage of the light curve during primary eclipse is not very good, the light curve is that of a typical EB type. Initially, we solved for the inclination, the secondary temperature, and the primary radius, fixing the secondary radius at the Roche-lobe value. However, we found that the light ratio of the solution was inconsistent with the spectroscopy, in the sense that the photometric ratio was much greater than that suggested by the spectroscopy. From the equivalent widths of the strongest absorption lines in the disentangled spectra we estimate a flux ratio of $\sim$2.5 at $\sim$ 4400Å. By fixing the secondary temperature (i.e., brightness) according to this light ratio we were able to obtain a satisfactory and consistent fit to the light curve, and solving only for the primary radius and the inclination. Secondary eclipse is fitted very well, but primary eclipse shows some asymmetry with the phases just before ingress being 0.02 mag fainter than egress.

3.4.6 6 215965

The light curve of this object has been analysed by Wyithe & Wilson (2001), who assumed a mass ratio of unity. They suggested that the system should be a good distance indicator on the grounds that it may show complete eclipses.

The S:N of our spectral observations of this target vary between 20 and 100 per pixel, with a median of about 50. The quadrature phases are well sampled, and features of both components are clearly seen in spectra obtained at these phases. The separated component spectra indicate a light ratio (p/s) of around 0.9.

The light curve shows relatively deep eclipses ($\sim$ 0.4 mag, with the secondary eclipse about 0.05 mag shallower – see Figure 3f). The entry ingress of the primary eclipse is quite poorly sampled, although the light-curve itself is of relatively high quality. There is considerable variability outside eclipses, indicating that the stars are significantly tidally distorted. We fitted for the inclination, the two relative radii, and the secondary temperature. This solution fitted the I-band light curve well, but returned a B-band flux ratio (p/s) of 1.3, which conflicts with the spectroscopic evidence of 0.9. It is most likely that the light curve solution has been compromised by the less well sampled sections of the eclipse curves. Therefore, we fixed the B-band flux ratio at 0.9, adopted a temperature for the secondary of 27800 K corresponding to its spectral type of B0.5, and calculated the radius of the secondary to provide the observed B-band flux ratio. Light-curve solutions for the primary radius and the inclination, with the secondary radius recalculated at each iteration then provided a final solution (Table 3) of the light curve that agrees with the spectroscopic data, and fits the light curve almost as well as the first solution for 4 parameters. The whole light curve is fitted reasonably well, particularly secondary eclipse, except for a $+0.007 \pm 0.012$(sd) mean (O-C) offset for the data within primary eclipse. The eclipses are partial in this solution.

Our light-curve solution is not consistent with that published by Wyithe & Wilson (2001), which (in the absence of spectroscopic data) was performed without a constraint on the light ratio.

3.4.7 7 243913

This system has $V = 14.8$, and the spectra obtained have a S:N between 20 and 40. The coverage is good at second quadrature (9 spectra), but is relatively poor at first quadrature (3 spectra only). The secondary's spectral features are 0.5 mag weaker than those of the primary.

The I-band light curve may be fitted equally well at a fixed spectroscopic mass ratio of 1.77 by either a detached configuration with the secondary cooler and smaller than the primary, or by a semi-detached configuration with the

Table 3. Light-curve solutions. Columns give the OGLE target designation; the nature of the system according to the adopted solution (detached, semi-detached, or contact); and then, for the primary and secondary stars, our spectral types; the (flux-averaged) effective temperatures; the mean stellar radii relative to the binary separation; the inclination; the component masses; the absolute mean radii; and the equivalent surface gravities ($GM/\overline{R}^2$). The primaries' temperatures are adopted on the basis of the adopted spectral types (cf. Section 6.1), and the secondary temperatures follow from the radii and primary:secondary intensity ratios at quadratures (Section 6.3).

Star Number	System type		Spectral type	Temperature (K)	Relative radius	Inclination (°)	Mass ($M_\odot$)	Radius ($R_\odot$)	$\log g$ dex (cgs)
5 038089	d	p	B0	30100 (fixed)	0.252 ± 0.005	76.9 ± 0.3	17.1 ± 1.5	6.1 ± 0.2	4.10 ± 0.05
		s	B0.2	29180 (fixed)	0.249 ± 0.008		19.1 ± 1.6	6.1 ± 0.3	4.15 ± 0.05
5 202153	s	p	O9.5	32200 (fixed)	0.257 ± 0.004	87.0 ± 0.2	19.9 ± 1.1	9.5 ± 0.3	3.78 ± 0.03
		s	B0.5	23450 ± 200	0.346 (fixed)		12.5 ± 1.2	12.8 ± 0.3	3.32 ± 0.04
5 316725	s	p	O9	33800 (fixed)	0.264 ± 0.007	77.6 ± 0.3	17.0 ± 1.5	6.1 ± 0.3	4.09 ± 0.05
		s	O9	31540 ± 170	0.330 (fixed)		8.9 ± 1.1	7.7 ± 0.2	3.62 ± 0.06
6 077224	s	p	O9.5	32200 (fixed)	0.283 ± 0.003	61.1 ± 0.2	15.9 ± 1.0	8.9 ± 0.3	3.74 ± 0.04
		s	B0.5	25710 ± 530	0.365 (fixed)		13.1 ± 1.4	11.5 ± 0.3	3.43 ± 0.05
6 158118	s	p	B0.2	29180 (fixed)	0.334 ± 0.004	69.2 ± 0.2	16.0 ± 0.7	7.6 ± 0.2	3.88 ± 0.02
		s	B1	18380 (fixed)	0.324 (fixed)		7.9 ± 0.5	7.4 ± 0.1	3.60 ± 0.03
6 215965	d	p	B0.5	27800 (fixed)	0.294 ± 0.004	75.6 ± 0.3	16.0 ± 0.5	9.9 ± 0.2	3.66 ± 0.02
		s	B0.5	27800 (fixed)	0.307 (fixed)		17.2 ± 0.8	10.4 ± 0.1	3.65 ± 0.03
7 243913	s	p	O9.5	32200 (fixed)	0.334 ± 0.003	73.3 ± 0.2	18.6 ± 1.1	8.2 ± 0.2	3.88 ± 0.03
		s	B1.5	25960 ± 310	0.336 (fixed)		10.5 ± 0.9	8.3 ± 0.2	3.62 ± 0.04
9 175323	c	p	O6.5	39250 (fixed)	0.418 (fixed)	58.0 ± 0.2	23.6 ± 1.6	10.2 ± 0.3	3.79 ± 0.04
		s	O7	38500 (fixed)	0.349 (fixed)		16.2 ± 1.5	8.5 ± 0.2	3.79 ± 0.04
11 30116	s	p	B0.5	27800 (fixed)	0.306 ± 0.003	83.8 ± 0.2	14.3 ± 1.9	7.4 ± 0.4	3.85 ± 0.08
		s	B2	20340 (fixed)	0.332 (fixed)		7.7 ± 1.9	8.1 ± 0.5	3.51 ± 0.12
11 57855	d	p	B0.5	27800 (fixed)	0.381 ± 0.006	65.6 ± 0.7	12.4 ± 1.1	5.2 ± 0.2	4.09 ± 0.05
		s	B1	25970 ± 930	0.272 ± 0.014		8.2 ± 1.3	3.7 ± 0.2	4.21 ± 0.09

secondary filling its Roche lobe at a radius comparable with that of the primary and at a higher temperature than in the detached case. However, the detached configuration suggests a B-band flux ratio of greater than 5, whereas the semi-detached configuration indicates a B-band flux ratio of 1.4, in excellent agreement with the spectroscopic data. This is a well-fitted light curve (a flat (O-C) curve) except for a short section of disparity just before ingress to primary eclipse.

3.4.8 9 175323

At $V = 13.7$ this is the brightest target in the present sample, and the spectroscopic data are of correspondingly good quality (S:N typically $\gtrsim 50$). Although the object was not in the overlap region of the 2dF fields, and hence there are currently only 16 phase points available, the orbit was fortuitously phased for our run, and 11 of the spectra were obtained near quadrature phases. The presence of very strong He II absorption and N III λ4634–40–42 emission indicates very luminous components, and we estimate spectral types of O6.5 and O7 for the primary and secondary respectively.

The I-band light curve strongly suggests a contact system, and attempts to secure solutions with a fill-out factor exceeding the Roche-lobe sizes were made, as for standard contact binaries. These solutions failed, with the code restoring the fill-out factor back to marginally separated stars. Accordingly, a semi-detached configuration was attempted with the B-band flux ratio of 1.3 being adopted from the spectroscopy to fix the secondary temperature. Solutions were made for the primary radius and the orbital inclination. We find that the primary component very nearly fills its Roche lobe (a filling factor of 99 per cent) and that the system is essentially in a marginal contact state. The (O-C) curve is flat through all orbital phases demonstrating a very good fit to the light curve. We note that the solution is very similar to two other well-studied systems, V348 Car (Hilditch & Lloyd-Evans 1985) and SX Aur (Bell, Adamson & Hilditch 1987).

3.4.9 11 30116

11 30116 has V magnitude of 14.7, and a S:N of 30 is typical of our spectroscopic data of this system. The star is not in the 2dF overlap region, although 13 of the 16 spectra were obtained near quadrature phases. The primary's spectral features are stronger than those of the secondary.

The I-band light curve is of the EB type, but the phase sampling of the photometry is poor during the middle of the secondary eclipse. From an initially detached description, the solutions converged rapidly to a semi-detached configuration. We therefore fixed the secondary radius at the Roche-lobe value, and at first solved for the secondary temperature, the inclination, and the primary radius. However, the solution gave a B-band light ratio of 2.3, which is inconsistent with the relative strength of the spectral lines. We therefore estimated the spectroscopic light ratio from the strengths of the strongest H/He lines, obtaining a value of 1.5 (p/s). The solution given in Table 3 was obtained by fixing the B-band light ratio at this value, and solving only for the primary radius and the inclination. Most parts of the light

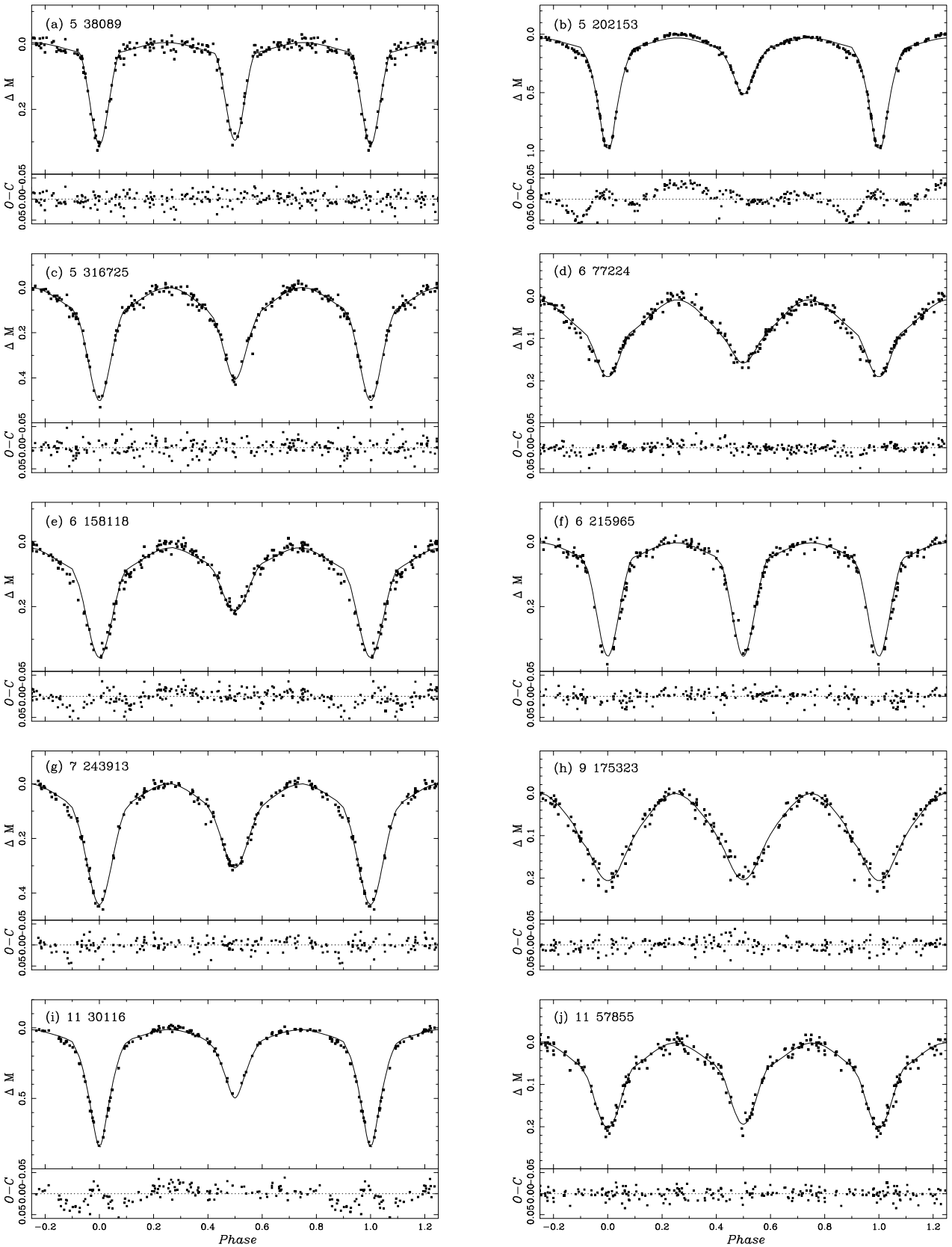

Figure 3. *I*-band light-curve fits for the sample, plotted over 1.5 cycles. Each panel shows the data (points) and fit (solid) line (upper subpanel), along with the $(O - C)$ scatter about the fit (lower subpanel). Note that the phases plotted here are *photometric*.

curve are fitted very well with some disparity before ingress to primary eclipse and through egress.

3.4.10 11 57855

This short-period system is the faintest of the ten considered here, and this is reflected in the quality of the spectra, which have a typical S:N of ∼20–30. The target is located outside the overlap region, in Field 2, and therefore has only 16 phase points in total, of which 7 were close to quadrature phases. We solved the light curve for the secondary temperature, the inclination and the two radii. The solution indicates a detached system, with the primary close to filling its Roche Lobe (92% by volume). This light-curve solution predicts a B-band flux ratio of 2.4 around the quadratures, in good agreement with the estimates from the spectroscopy of 2.0-2.5. The (O-C) curve is flat through all orbital phases demonstrating a very good fit to the light curve.

4 EVOLUTIONARY CHARACTERISTICS

4.1 Detached systems

Since our sample is limited to $P_{\rm orb} < 5$d, it is unsurprising that only 3 of the 10 systems are detached. The B0+B0.2 system 5 38089 has a period of 2.4 d and component masses of $17.1 \pm 1.5 {\rm M}_{\odot}$ and $19.1 \pm 1.6 {\rm M}_{\odot}$. Both stars are well within their Roche lobes, with volume-filling factors of 69% and 64% for the primary and secondary, respectively.

The longer-period system 6 215965 ($P_{\rm orb} = 3.9$d) contains two B0.5 stars, and is both slightly more evolved (see Figure 4) and of similar mass ($16.0 \pm 0.5 {\rm M}_{\odot}$ for the primary and 17.2 ± 0.8 for the secondary). Since its mass ratio is close to unity this system does not critically test the evolution models.

The short-period system 11 57855 contains an 12.4±1.1-$\rm M_{\odot}$, B0.5 primary and a 8.2 ± 1.3-$\rm M_{\odot}$, B1 secondary, and this larger mass ratio means this system offers a better test of the models.

We plot these systems in the mass–surface-gravity plane in Figure 4(a), along with the $Z = 0.004$ evolutionary tracks by Girardi et al. (2000). It appears that 6 215965 is approximately 10 Myr old, whereas 5 038089 is younger (around 5 Myr). Both components of 11 57855 lie on the 10 Myr isochrone, although the gravity of the secondary is quite poorly constrained (due to a relatively large error on the relative radius of the secondary from the light-curve fit). Analysis of further systems should reveal more detached binaries with $q > 1$, which may be used to test critically the models.

4.2 Semi-detached systems

Six of the ten systems presented here are in a semi-detached configuration in which the secondary star fills its Roche lobe. We believe that these systems evolved to this state via case-A mass transfer, in which the mass donor (now the less massive star) reached its Roche lobe whilst on the main sequence, and that the stars are now in the slow phase of case-A mass transfer (Wellstein, Langer & Braun 2001). As expected, the secondary (mass-donor) stars are now overluminous for their spectral types, while the primary stars (the mass gainers) appear as slightly evolved main-sequence objects (see Figure 4b).

The mass donors typically have masses of 6–8$\rm M_{\odot}$, which is in good agreement with the masses found for galactic semi-detached OB-star binaries (see, for example, Figure 9 of Harries et al. 1998).

5 THE DISTANCE TO THE SMC: PREAMBLE

In order to reveal clearly the central arguments which lead to the distance estimates for our sample, and potential sources of error and uncertainty, we first review the key steps.

5.1 Light-curve analysis

The quantities of interest which are obtained from the light-curve analysis are the stellar radii, scaled to the size of the orbit; the orbital inclination; and, essentially, the ratio of surface brightnesses of the two components. (In the absence of gravity darkening, limb darkening, tidal distortions and reflection, the ratio of eclipse depths gives the surface-brightness ratio directly.) This ratio is conveniently expressed in terms of stellar temperatures, but it is important to recall that, for practical purposes, a light-curve obtained in a single colour carries no direct information on the actual temperatures. The corollary to this is that the dimensional information obtained from the light-curves (and our discussion to this point) are essentially independent of the adopted temperature scale.

The light-curve solutions conducted here use well-established physics encoded in mature software. It is reasonable to suppose that the light-curve analysis is not a source of significant systematic errors.

5.2 Radial-velocity analysis

The radial-velocity solution, together with the inclination from the light-curve analysis, yields the size of the orbit (and hence places the stellar radii on an absolute scale), and the stellar masses. Although the measurement techniques adopted herein have been developed relatively recently, they seem robust, and hence it is again reasonable to suppose that the radial-velocity orbits are not a source of significant systematic errors.

5.3 Absolute magnitudes and extinction

Given the radius of a star, a knowledge of its surface brightness in some photometric passband allows its absolute magnitude in that passband to be calculated. The apparent magnitude, corrected for interstellar extinction, then gives the distance. The calculation of surface brightness and the determination of the extinction are crucial factors (and important sources of potential systematic errors) and are discussed in detail in the following sections. (Of course, the temperature and surface brightness vary across the surface of a star in a binary system, and we take proper account of that in our calculations.)

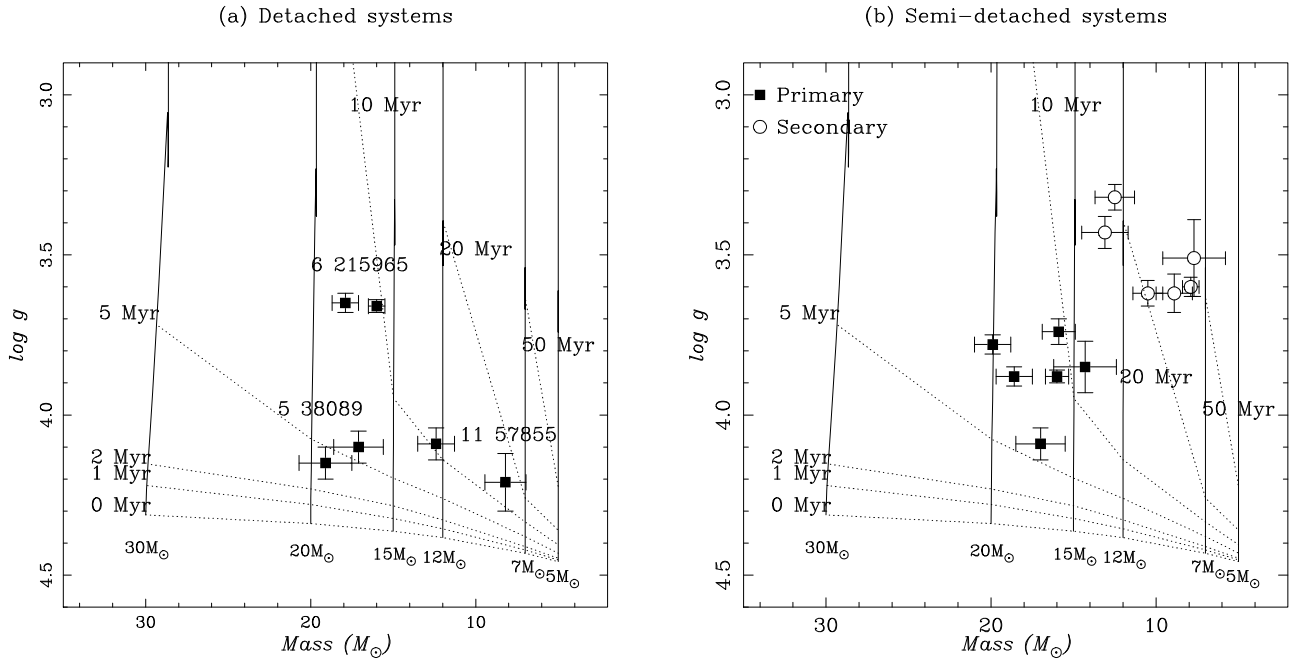

Figure 4. The parameters of (a) the detached and (b) the semi-detached systems, plotted in the mass–log g plane. For the detached systems the components are plotted as filled squares, while for the semi-detached systems the primaries are plotted as filled squares and the secondaries as open circles. Evolutionary tracks for different masses ($Z = 0.004$; Girardi et al. 2000) are plotted for different masses (solid lines), along with isochrones for 0, 1, 2, 5, and 10 Myr (dotted lines).

6 ABSOLUTE-MAGNITUDE CALCULATIONS

To determine the stellar surface brightness requires the assignment of an effective temperature, and the calculation of a model atmosphere to give the emergent flux as a function of wavelength.[2] For stars somewhat cooler than those considered here, it may be possible to make a direct estimate of the stellar temperatures from observed continuum fluxes (e.g., Guinan et al. 1998), although even this approach entails significant uncertainties (cf. Groenewegen & Salaris 2001). In our case, we have to rely on a simple calibration of temperature as a function of spectral type.

6.1 Temperature scales

Because much of the radiation of O- and early B-type stars is emitted in unobservable spectral regions,[3] and because the slope of the optical continuum is insensitive to temperature for these stars, spectroscopic $T_{\rm eff}$ determinations must rely heavily on modeling of the line spectra (in practice, He I/He II line ratios). 'Traditional' temperature scales, exemplified by those given by Conti (1973) and Howarth & Prinja (1989), are based on relatively simple non-LTE H/He models. Subsequent work using line-blanketed nLTE models (e.g., Hubeny, Heap & Lanz 1998) and the independent technique of comparison of fundamental stellar parameters with evolutionary models (Hilditch et al. 1996; Harries & Hilditch 1998) suggest that the simple models lead to temperatures which are systematically too high, at a level of ∼1kK.

Table 4 summarises a number of temperature scales that have been published in the 'nLTE era'. In spite of the difficulties alluded to above, there is a reasonable degree of agreement for main-sequence stars, results being bracketed by the Vacca, Garmany & Shull (1996) scale, which is the hottest at all spectral types, and the Böhm-Vitense (1981) scale, which is generally the coolest. We require a calibration that covers both late-O and early-B subtypes, and adopt as a starting point the results given by Böhm-Vitense (1981).

This is a rather venerable scale which, at these temperatures, is derived in large part from studies by Conti (1973) and by Underhill et al. (1979), which in turn are not above criticism (being based on unblanketed models, and continuum-fitting techniques, respectively). Nonetheless, the Böhm-Vitense scale is in good agreement with more recent analyses (at least for near-main-sequence stars), and, in particular, by adopting a relatively 'cool' scale we acknowledge the trends indicated by the binary-star and line-blanketed work. Moreover, across the O9–B1 range, where most (80%) of our stars occur, the temperature span of the Böhm-Vitense scale, 8.2kK, is greater than that of other scales. We present an argument in Section 6.4 that this is a desirable characteristic.

The Böhm-Vitense calibration (in common with all oth-

[2] It may appear that a short-cut can be achieved by using the bolometric correction. That is, given the stellar radius and temperature, one has the luminosity, hence $M_{\rm BOL}$; the effective temperature also yields the bolometric correction, hence $M(V)$. However, the bolometric correction is, in effect, a parameterization of the V-band surface brightness, and is strongly model dependent for stars such as those considered here, where the greater part of the emitted flux emerges at unobservable wavelengths.

[3] More than 90% of the flux of a 30kK, $\log g = 4.0$ SMC-metallicity model emerges at wavelengths shortwards of 300nm.

Table 4. Selected spectral-type–$T_{\rm eff}$ calibrations for late-O and early-B dwarfs in units of kK. Sources are Conti (1973; nLTE H/He models); Böhm-Vitense (1981; semi-direct, and nLTE H/He); Underhill (1982; semi-direct); Schmidt-Kaler (1982; semi-direct, and nLTE H/He); Howarth & Prinja (1989; nLTE H/He); Vacca, Garmany & Shull (1996; nLTE H/He); Crowther (1997, updated; various); Martins et al. (2002; unblanketed [u] and line-blanketed [ℓ] nLTE models). Not all scales use independent primary data – e.g., the BV81 and SK82 scales both incorporate the C73 results. The adopted SMC scale is discussed in Section 6.1

	C73	BV81	U82	SK82	HP89	VGS	PAC	MSHu	MSHℓ	Adopted	
O6	42.0	39.0		41.0	42.0	43.6	42.0	42.0	39.5	40.0	O6
O6.5	40.0				40.5	42.3		40.5	38.2		O6.5
O7	38.5	37.5		38.0	39.0	41.0	40.0	39.5	37.0	38.5	O7
O7.5	37.5				37.5	39.7		38.5	36.0		O7.5
O8	36.5	35.6		35.8	36.5	38.4	35.0	37.0	35.2	36.3	O8
O8.5	35.5	34.6			35.0	37.2		36.2	34.5	35.3	O8.5
O9	34.5	33.2		33.0	34.0	35.9	31.8	35.5	34.0	33.8	O9
O9.5	33.0	31.6			33.0	34.6	30.8	34.5	33.0	32.2	O9.5
B0		29.5	30.8	30.0		33.3	29.8			30.1	B0
B0.5		27.3	29.3			32.1	28.5			27.8	B0.5
B1		25.0	26.9	25.4			26.1			25.5	B1
B1.5		23.0	25.7				24.8			23.5	B1.5
B2		21.5	22.8	22.0			21.3			21.9	B2

Table 5. Surface-brightness characteristics of model atmospheres. Models are identified by origin and $\log g$ (cgs, $\times 10$): A (ATLAS9 solar-metallicity line-blanketed models), S (Howarth & Lynas-Gray 1989, SMC-metallicity line-blanketed ATLAS6 models), T (Smith & Howarth 1998, TLUSTY nLTE H/He models), and BB (black-body).

Model	$\partial \ln S/\partial T_{\rm eff}$ [kK^{-1}]	$S(I)$ at 30kK [10^7 erg cm^{-2} s^{-1} Å^{-1}]
A35	6.8×10^{-2}	11.8
A40	6.5×10^{-2}	11.1
S35	6.7×10^{-2}	11.0
S40	6.5×10^{-2}	10.4
T40	6.1×10^{-2}	9.9
BB	4.5×10^{-2}	14.0

ers) relates the temperatures of *Galactic* stars to their spectral types. Even though the spectral types of our stars are largely based on their helium spectra, and hence are effectively independent of metallicity, it would not be surprising if given helium-line ratios were obtained at different effective temperatures for Galactic and SMC metallicities. Unblanketed models offer no direct insight into the magnitude of such differences, but Martins, Schaerer & Hillier (2002) report that temperature differences between unblanketed models and line-blanketed models with SMC metallicity are ∼60% of those between unblanketed and Galactic models.

In adopting an SMC temperature scale, we therefore increase the Böhm-Vitense temperatures by 40% of the temperature differences implied by the Martins et al. unblanketed and (Galactic-metallicity) blanketed models. For late-O stars this leads to an increase in temperature of ∼0.6kK, or ∼2% of $T_{\rm eff}$, a scale factor which we also apply to the B-star scale. We will consider the consequences of the adopted scale further when discussing the error budget.

6.2 Surface brightness

We have examined the surface brightness, S, as a function of temperature over the range 25–35kK by using a grid of ATLAS9 line-blanketed, solar-metallicity, LTE models (Kurucz 1993); the Howarth & Lynas-Gray (1989) line-blanketed, ∼SMC-metallicity, LTE models; and the Smith & Howarth (1998) nLTE H/He models. The models were convolved with the photometric passbands given by Bessell (1990).

For all models, we find $\partial \ln S/\partial T_{\rm eff} = 6$–$7 \times 10^{-2}$ kK^{-1} (and $\partial \ln S/\partial \log g \simeq -0.1$) in the I band at ∼30kK. The magnitude of this dependence increases with decreasing wavelength, indicating that for our purposes it is preferable to work at I rather than at B or V. (The effects of extinction are also less at longer wavelengths.)

There is a significant (∼10%) dispersion in the I-band surface brightness between models; with decreasing line blanketing the surface brightness decreases (simply because more flux can escape at shorter wavelengths). At ∼30kK, the I-band surface of a Howarth & Lynas-Gray (SMC-metallicity) model is matched by that of an ATLAS9 model ∼1kK cooler, and by a Smith & Howarth model ∼1kK hotter.

We adopt the Howarth & Lynas-Gray model fluxes as the most appropriate for our purposes. While these LTE models are not suitable for line-profile analyses, we expect them to give a reasonable representation of the optical and near-IR continuum fluxes for late-O/early-B main-sequence stars.

6.3 Methodology and results

The LIGHT2 code used for the light-curve analysis uses modified black-body fluxes in its calculations, and is accordingly not suitable for predicting stellar absolute magnitudes directly. We therefore took the best-fit parameters found by using LIGHT2, and applied them to a separate synthesis code, SHADE (Howarth & Wilson 1983). This code incorporates essentially the same standard physics as LIGHT2, but al-

Table 6. Photometric data. The calculation of the absolute I_C magnitudes at quadratures, $M(I)$, is described in Section 6.3. The quoted $E(B-V)$ reddenings are calculated as $E(B-I)/2.3$, as discussed in Section 7. I_0 is the dereddened I magnitude at quadrature, and DM the true distance modulus.

Star	$M(I)$	$B-I$	$E(B-V)$	$A(I)$	I_0	DM
5 038089	−3.87	−0.37	0.10	0.18	15.04	18.92
5 202153	−5.05	−0.36	0.10	0.18	14.08	19.13
5 316725	−4.36	−0.40	0.09	0.16	14.53	18.90
6 077224	−4.98	−0.28	0.14	0.25	13.76	18.73
6 158118	−4.00	−0.24	0.16	0.28	14.78	18.77
6 215965	−4.86	−0.41	0.08	0.15	13.97	18.83
7 243913	−4.52	−0.25	0.15	0.28	14.58	19.10
9 175323	−5.31	−0.41	0.08	0.15	13.53	18.84
11 30116	−4.01	−0.37	0.10	0.18	14.70	18.71
11 57855	−3.03	−0.45	0.07	0.12	15.88	18.92

lows more freedom in the choice of model-atmosphere grids.[4] Fluxes are interpolated linearly in $\log T_{\rm eff}$ and $\log g$, in this case for grids sampled every 2kK, 0.5 dex. We converted from fluxes to magnitudes using the zero-point calibrations given by Bessell et al. (1998; note that the f_λ and f_ν zero-points are transposed in their Table A2).

The procedure adopted was to match the mean radius of the primary, as determined using LIGHT2, and its mean temperature (assigned on the basis of spectral type), and thereby to compute its I-band flux at quadrature. The radius of the secondary was then set at the LIGHT2 value, and the temperature adjusted until the primary:secondary quadrature flux ratio matched that determined by the light-curve synthesis. Since it is fundamentally the flux ratio, not the relative temperatures, which is determined in the light-curve synthesis, this is the most transparent and direct procedure for determining the secondary temperatures and absolute fluxes.

The results on temperatures are included in Table 3 (where the errors on the secondary temperatures propagate from the intensity ratios, and are therefore *internal* errors), and the computed absolute magnitudes are given in Table 6.

6.4 Temperatures revisited

The secondary temperatures estimated from flux ratios may now be compared with the temperatures implied by the spectral types.

The secondary temperatures required to match the observed primary:secondary flux ratios appear systematically lower than the temperatures implied by the spectral types, by 2.1 ± 3.1kK ($8 \pm 12\%$ s.d.) on average. That is, the temperature differences between the primaries and secondaries as indicated by their spectral types are, on average, smaller than the temperature differences indicated by their surface-brightness ratios. Obviously, a more 'compressed' temperature scale than the adopted one (i.e., a scale in which the temperature difference between adjacent spectral types is smaller) would exacerbate this problem.

The simplest (but not the only) interpretation is that the secondaries' line spectra indicate spectral classifications

[4] SHADE does not allow both stars to be modelled simultaneously, which is why it could not be used for the light-curve modelling.

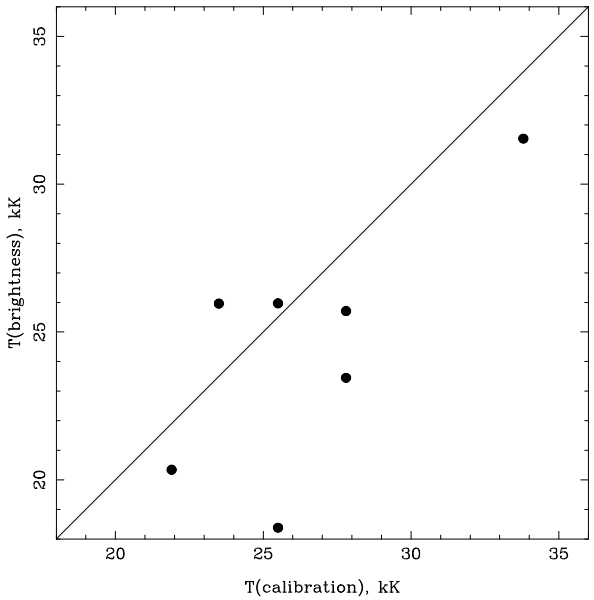

Figure 5. Comparison of secondary-star effective temperatures inferred from spectral types ('calibration' temperatures) and from surface brightnesses.

∼1 subtype earlier than do their I-band continuum fluxes. A possible explanation is that this is a consequence of the 'reflection effect', i.e., that the outer, line-forming regions of the secondary atmospheres are heated by the incident radiation of the primary.

7 EXTINCTION

Interstellar reddening towards and within the SMC has been considered by many authors, with a consensus that fairly small values of $E(B-V)$ generally apply. Older studies are summarized by McNamara & Feltz (1980) and by Bessell (1991), who advocate foreground (and therefore minimum) reddenings of $E(B-V) = 0.02$ and 0.05, respectively. More recent work indicates reddenings of ∼0.05–0.25. (e.g., Hill, Madore & Freedman 1994; Massey et al. 1995; Dutra et al. 2001; Zaritsky et al. 2002). The OGLE data for our targets

are in good agreement with these results, as expected from the claimed photometric accuracy of ∼0.01 mag (Udalski et al. 1998).

To investigate reddenings and extinctions to our targets, we assume that the intrinsic colours of Galactic stars apply to our SMC targets (the differences in these colours between Kurucz solar-metallicity and SMC-metallicity models are negligible), and that the optical–near-IR extinction curve is also similar (e.g., Feast & Whitelock 1984; Gordon & Clayton 1998).

In principle, we want to use the longest available wavelength baseline to determine reddenings – i.e., $(B-I)$. Writing $x = E(V-I)/E(B-V)$ and $R_V = A(V)/E(B-V)$, in order to show explicitly the dependence of extinction on these quantities, we then have

$$A(I) = \frac{E(B-I)}{1+x}(R_V - x). \quad (4)$$

Unfortunately, although it is well established that Galactic late-O/early-B near-main-sequence stars have $(B-V)_0 \simeq -0.30$ (Fitzgerald 1970; Ducati et al. 2001), the intrinsic $(V-I)$ colours are much more poorly determined. We therefore estimate $\overline{(V-I)}_0$ for our stars from the OGLE data by noting that

$$(V-I)_0 = (V-I) - x\left((B-V) - (B-V)_0\right),$$

finding $\overline{(V-I)}_0 = -0.30$ (i.e., $(B-I)_0 = -0.60$) for $x = 1.30$, $(B-V)_0 = -0.30$. This compares favourably with values of -0.28 and -0.33 reported by Wegner (1994) and by Ducati et al. (2001), after conversion from $(V-I)_{\rm J}$ to $(V-I)_{\rm C}$ using the transformation given by Cousins (1980).

The adopted I-band extinctions for our targets were calculated by using eqtn. 4, adopting $E(B-I) = (B-I)+0.60$ together with $R_V = 3.1$, and $x = 1.30$ (Howarth 1983; Cardelli, Clayton & Mathis 1989; Mathis 1990). Results are included in Table 6. Note that by adopting the $(B-I)$ reddenings to determine the crucial quantity $A(I)$, we are not improving the external *accuracy* of the results (which is established from the $(B-V)$ colours); but that the internal *precision* is considerably improved by using more than a threefold increase in wavelength baseline.

The mean reddening towards our targets is $\overline{E}(B-V) = 0.11$, with an s.d. of 0.03 (range 0.07–0.16). A complementary indicator of the consistency of the adopted reddenings can be obtained by comparing two estimates of $E(B-V)$, viz. $(B-V)+0.30$ and $[(B-I)+0.60]/[1+x]$ for the sample. The mean difference is zero (by construction), with an s.d. of 0.021.

8 THE DISTANCE TO THE SMC

The previous sections describe our determinations of the calculated absolute I-magnitudes at quadratures (Section 6.3) and I-band extinctions (Section 7). Combined with the observed I-band quadrature magnitudes, these data yield the true distance moduli directly. The quadrature magnitudes come from the normalizations of the light-curve models, and are included in Table 1; the distance moduli are given in Table 6. The average true distance modulus to our targets, for the adopted temperature scale, is found to be 18.89 ± 0.14 (s.d.; error on the mean 0.04).

Although we can determine the distances to our targets with reasonable precision, we need to consider their location within the SMC in order to derive 'the' distance. The dynamics and structure of the SMC are complex, probably as a result of interaction with the LMC (Murai & Fujimoto 1980; Gardiner & Noguchi 1996), and that structure is, arguably, still not completely clear. Caldwell & Coulson (1986), Laney & Stobie (1986), and Mathewson et al. (1988) found line-of-sight depths of ∼20 kpc, while Welch et al. (1987) concluded that the dispersion of the Cepheid period–luminosity(–colour) relation corresponds to a depth of only 3.3kpc; Martin, Maurice & Lequeux (1989) similarly concluded that most of the young population lie within a band less than 10kpc deep, as did Crowl et al. (2001). Gardiner, Hatzidimitriou, Hawkins, and collaborators have conducted a complementary series of studies of the outer regions of the SMC (e.g., Hatzidimitriou, Cannon & Hawkins 1993, and references therein).

Part of the discrepancy between different papers appears to arise because of different interpretation of what 'the' depth actually means. Our digest of published work is that the bulk of the young populations at the centre of the SMC have a line of sight depth of less than 10kpc; the main body of the bar is closer in the NE and more distant in the SW, by ∼0.2 mag in distance modulus (Mathewson et al. 1988; Gardiner & Hawkins 1991).

Our target fields are less than 1° from the optical and dynamical centres of the SMC. The distance we find for our targets should therefore be directly representative of the mean distance of the SMC. Moreover, the modest line-of-sight depth at this location means that our sample should not be significantly biased towards near-side objects (intrinsic luminosity, and variable transmission through the 2dF fibre feeds, will be more important in determining which targets have good S:N than will fore-and-aft location within the Cloud).

Our distances are formally consistent with all targets lying at a common distance. However, the two targets 5 202153 and 7 243913 are distance outliers in the distribution, and hint at a real depth effect, although their radial velocities, which might be expected to reflect any distinct dynamical properties, are unexceptional (Table 2). Their discrepant distances cannot result directly from the surface-brightness calibration, as these systems have spectral types which fall in the main grouping of targets.

Finally, we note that our internal error estimates, discussed below, are commensurate with the dispersion in distances to individual systems, which provides the ultimate validation of our procedures.

8.1 Error budget

8.1.1 Systematic errors

Since reddenings are generally small, extinction is unlikely to be an important source of systematic error; for example, the sensitivity of true distance modulus to R_V, the ratio of selective to total extinction, is $\partial_{\rm DM}/\partial R_V = 0.1$ at I. For SMC (internal) reddening of $E(B-V) = 0.1$, which is at the upper end of the range found for our targets, even a systematic error in R_V as large as 0.5 (the extreme range of

results given by Gordon & Clayton 1998) would change the true distance modulus by only 0.05.

Individual $E(B-V)$ reddening estimates are unlikely to be *systematically* in error unless SMC stars of a given spectral type have significantly different intrinsic colours to their Galactic counterparts. Model-atmosphere calculations, and observations, provide no indication that this is the case.

The flux calibration of the magnitude scale (a source of systematic error which affects all photometrically-based distance estimates) is uncertain at the $\sim 1\%$ level.

Potentially, our most important source of systematic error is the adopted temperature–spectral-type scale (and the associated relationship between surface brightness and effective temperature). The spread in temperature scales is $\sim$1–2kK for late-O to early-B types, which provides some guidance to the magnitude of systemetic errors in this factor (although consistency may be a poor guide to correctness). For every 1kK change in $T_{\rm eff}$, there is a $\sim$7% change in surface brightness, or a $\sim$3% change in distance d (0.06 mag in distance modulus).

Considering these factors, a reasonable estimate of the maximum systematic error in the mean distance modulus from our (ultimately large) sample is $\sim$0.1. A hotter temperature scale would lead to an increased distance estimate, as would (to a lesser extent) a decrease in the SMC value of R_V.

8.1.2 Random errors

By random errors we mean the statistical uncertainty on the estimated distance to a single system. This uncertainty results from errors on the stellar radii; temperatures; and reddenings.

Since we essentially measure an angular diameter, errors on the radii correlate directly with errors on distance. These errors are explicitly considered in the errors quoted in Table 3; a typical $\sim$4% uncertainty in radius R corresponds to an equal uncertainty in d.

The spectral classifications of the primaries are estimated to be good to $\sim$1 subtype; at O9-B0.5, this corresponds to an error of $\sim 1\frac{1}{2}$kK in $T_{\rm eff}$ which, as noted above, corresponds to a $\sim$5% error in distance.

The observational determination of quadrature magnitudes is not a significant source of error (the light-curve normalizations are good at the millimagnitude level).

Finally, an error of 0.02m in $E(B-V)$ corresponds to an error of 0.06 in distance modulus, or 3% in d.

Adding these factors in quadrature, we conclude that the stochastic error on the distance to a well-observed system is typically $\sim$7% (0.15 mag in distance modulus).

9 DISCUSSION

The distance to the SMC has been measured using a variety of methods, although the most frequently adopted techniques are the Cepheid period–luminosity (PL) relation and, more recently, the red-clump method (see Table 7). The Cepheid period-luminosity relation has the advantage that the observations themselves are relatively straightforward, but the method requires a zero-point calibration (there are no reliable *Hipparcos* parallaxes of Cepheids; e.g., Madore & Freedman 1998), and the PL relation may have a metallicity dependence (e.g., Sasselov et al. 1997; Caputo et al. 2000). Despite these uncertainties, and although it does not provide a *primary* distance indicator, the Cepheid method remains a crucially important rung in the cosmic distance ladder, and is the foundation upon which the Hubble Key Project builds its measurement of H_0 (Freedman et al. 2001). Recent determinations of the distance modulus to the SMC using the PL relationship range from 18.84 (Böhm-Vitense 1997) to 19.11 (Visvanathan 1985; Groenewegen 2000; Bono, Caputo & Marconi 2001), and, broadly speaking, establish the 'long' distance scale.

Table 7. Recent distance determinations to the SMC.

Method	DM	Author
Period–luminosity-based methods		
IR Cepheid PL	19.11 ± 0.07	Visvanathan (1985)
Cepheid PL	18.97 ± 0.07	Caldwell & Coulson (1986)
Cepheid PL	18.93 ± 0.05	Welch et al. (1987)
Cepheid PL	18.84 ± 0.10	Böhm-vitense (1997)
Cepheid PL	19.11 ± 0.11	Groenewegen (2000)
$2^{\rm nd}$ overtone Cep	19.11 ± 0.11	Bono et al. (2001)
RR Lyr	18.78 ± 0.2	Reid & Strugnell (1986)
RR Lyr	18.66 ± 0.16	Udalski (1998a)
Red clump star methods		
Red clump	18.56 ± 0.06	Udalski et al. (1998a)
Red clump	18.82 ± 0.2	Cole (1998)
Red clump	18.91 ± 0.18	Twarog et al. (1999)
Red clump	18.77 ± 0.08	Popowski (2000)
Other methods		
Eclipsing binary	18.6 ± 0.3	Bell et al. (1991)
Cepheid brightness	18.9 ± 0.2	Barnes et al. (1993)
Tip RGB	18.99 ± 0.08	Cioni et al. (2000)
CMD fitting	18.88 ± 0.08	Dolphin et al. (2001)

The red-clump (RC) stars are metal-rich analogues of horizontal-branch stars, whose luminosity is thought to be independent of their age and chemical composition (to first order), so that they may be used as standard candles. One of the advantages of RC method is that it is developed from reliable *Hipparcos* parallaxes. The first application of the RC method to the SMC yielded a surprisingly short DM of 18.6 (Udalski et al. 1998a). Later studies by Cole (1998) and Twarog et al. (1999) invoked age and metallicity dependencies of the RC stars, yielding slightly longer distances (Table 7), but still somewhat shorter than the Cepheid scale. Although Udalski (1998b) proposed that the I-band metallicity dependence is weak, and that the RC luminosity is independent of age for stars 2–10 Gyr old, modeling of RC populations (Girardi & Salaris 2001) suggests that the situation may be complex, with a full calibration of the RC distance scale requiring knowledge of the star-formation history and the age–metallicity relation.

The distance modulus derived here (18.89 ± 0.04 mag) bisects the 'short' (red clump) and 'long' (Cepheid) characterisitic distances, and is in good agreement with, but more precise than, the Dolphin et al. (2001) measurement from CMD fitting (see Fig. 6 for a graphical comparison of recent distance estimates). We are continuing with the analysis of the remainder of our sample, although further spectroscopic observations will be necessary for complete quadrature phase coverage of all our objects. The final result of this

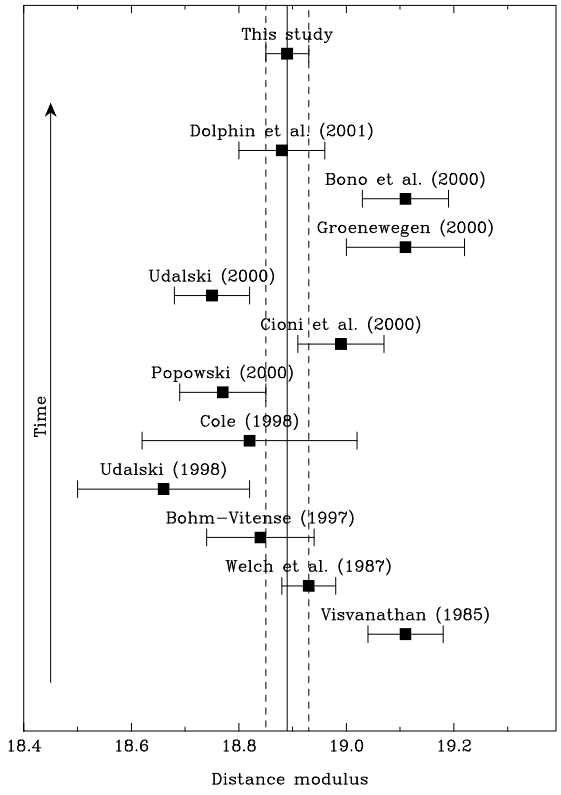

Figure 6. Distance moduli to the SMC calculated using a variety of techniques (see Table 7). The DM are plotted as filled squares with 1σ-error bars. The distance modulus derived from this study is shown for comparison with the dotted lines delineating the 1σ random error limit.

programme will be a substantial database of stellar parameters with which to test stellar evolution models (both single and binary). We will also be able to refine our distance estimate, and to examine further the three-dimensional structure of the central regions of the SMC.

ACKNOWLEDGEMENTS

This paper is based on data obtained by using the Anglo-Australian Telescope. Terry Bridges is warmly thanked for his expert help with the 2dF astrometry, for conducting the observations, and for his data reduction advice. We are grateful to the OGLE team for making their excellent photometric database publically available, and Graham Hill for the use of his LIGHT2 code.

REFERENCES

Barnes, T.G., Moffett, T.J., Gieren, W.P., 1993, ApJ, 405, L51
Bell, S.A., Adamson, A.J., Hilditch, R.W., 1987, MNRAS, 224, 649
Bell, S.A., Hilditch, R.W., Clausen, J.V., Reynolds, A.P., Giménez, A., 1991, MNRAS, 250, 119
Bessell, M.S., 1990, PASP, 102, 1181
Bessell, M.S., 1991, A&A, 242, L17
Bessell, M. S., Castelli, F., Plez, B., 1998, A&A, 333, 231
Böhm-Vitense, E., 1981, ARA&A, 19, 295
Böhm-Vitense, E., 1997, AJ, 113, 13
Bono, G., Caputo, F., Marconi, M., 2001, MNRAS, 325, 1353
Byrd, R.H., Lu, P., Nocedal, J., Zhu, C., 1995, Scientific Computing, 16, 1190
Caldwell, J.A.R., Coulson, I.M., 1986, MNRAS, 218, 223
Caputo, F., Marconi, M., Musella, I., Santolamazza, P., 2000, A&A, 359, 1059
Cardelli, J.A., Clayton, G.C., Mathis, J.S., 1989, ApJ, 345, 245
Charbonneau, P., Knapp, B., 1995, NCAR Technical Note, TN-418+IA
Cioni, M.-R.L.,van der Marel, R.P., Loup, C., Habing, H.J., 2000, A&A, 359, 601
Cole, A., ApJ, 1998, 500, L137
Conti, P.S., 1973, ApJ, 179, 181
Crowl, H.H., Sarajedini, A., Piatti, A.E., Geisler, D., Bica, E., Clariá, J.J., Santos, J.F.C., Jr., 2001, AJ, 122, 220
Crowther, P.A., 1998, IAU Symposium No. 189, Fundamental Stellar Properties: The Interaction between Observation and Theory, T.R. Bedding, A.J. Booth & J. Davis (eds), Kluwer, Dordrecht
Cousins, A.W., 1980, SAAO Circ., 1, 234
Dolphin, A.E., Walker, A.R., Hodge, P.W., Mateo, M., Olszewski, E.W., Schommer, R.A., Suntzeff, N. B., 2001, ApJ, 562, 303
Ducati, J.R., Bevilacqua, C.M., Rembold, S.B., Ribeiro, D., 2001, ApJ, 558, 309
Dutra, C.M, Bica, E., Clariá, J.J., Piatti, A.E., Ahumada, A.V., 2001, A&A, 371, 895
Fitzgerald, M.P., 1970, A&A, 4, 234
Fitzpatrick, E.L., Ribas, I., Guinan, E.F., DeWarf, L.E., Maloney, F.P., Massa, D., 2002, ApJ, 564, 260
Feast, M.W., Whitelock, P.A., 1984, The Observatory, 104, 193
Freedman, W.L., Madore, B.F., Gibson, B.K., et al., 2001, ApJ, 553, 47
Gardiner, L.T., Hawkins, M.R.S., 1991, MNRAS 251, 174
Gardiner, L.T., Noguchi, M., 1996, MNRAS, 278, 191
Girardi, L., Bressan, A., Bertelli, G., Chiosi, C., 2000, A&AS 141, 371
Girardi, L., Salaris, M., 2001, MNRAS, 323, 109
Gordon, K.D., Clayton, G.C., 1998, ApJ, 500, 816
Guinan, E.F., Fitzpatrick, E.L., Dewarf, L.E., Maloney, F.P., Maurone, P.A., Ribas, I., Pritchard, J.D., Bradstreet, D.H., Giménez, Á., 1998, ApJ, 509, L21
Groenewegen, M.A.T., 2000, A&A, 363, 901
Groenewegen, M.A.T., Salaris, M., 2001, A&A, 366, 752
Harries, T.J., Hilditch, R.W., Hill, G., 1997, MNRAS, 285, 277
Harries, T.J., Hilditch, R.W., 1998, in Boulder-Munich II: Properties of Hot, Luminous Stars (I.D. Howarth, ed.), ASP, p. 401
Harries, T.J., Hilditch, R.W., Hill, G., 1998, MNRAS, 295, 386
Hatzidimitriou, D., Cannon, R.D., Hawkins, M.R.S., 1993, MNRAS 261, 873
Hilditch, R.W., 2001, An Introduction to Close Binary Stars , CUP, p. 258
Hilditch, R.W., Lloyd-Evans, T., 1985, MNRAS, 213, 75
Hilditch, R.W., Harries, T.J., Bell, S.A., 1996, A&A, 314, 165
Hill, G., 1979, Publ. Dom Astrophys. Obs., 15, 297
Hill, G., Rucinski, S.M., 1993, in Milone, E.F. (ed), Light Curve Modeling of Eclipsing Binary Stars. Springer-Verlag (New York), p. 135
Hill, R.J., Madore, B.F., Freedman, W.L., 1994, ApJ, 429, 192
Holmgren, D.E., Hill, G., Fisher, W.A., 1990, A&A, 231, 409
Howarth, I.D., 1982, MNRAS, 198, 289
Howarth, I.D., Wilson, R., 1983, MNRAS, 202, 347
Howarth, I.D., Lynas-Gray, A.E., 1989, MNRAS, 240, 513
Howarth, I.D., Prinja, R.K., 1989, ApJS, 69, 527

Hubeny, I., Heap, S.R., Lanz, T., 1998, in Boulder-Munich II: Properties of Hot, Luminous Stars (I.D. Howarth, ed.), ASP, p. 108
Kopal, Z., 1959, Close binary systems, Chapman & Hall (London)
Kurucz, R.L., 1993, CD-ROM No. 13. Smithsonian Astrophysical Observatory, Cambridge, Mass.
Laney, C.D., Stobie, R.S., 1986, MNRAS, 222, 449
Lennon, D.J., 1997, A&A, 317, 871
Lewis, I.J., Cannon, R.D., Taylor, K., et al., 2002, MNRAS, 333, 279
McNamara, D.H., Feltz, K.A., Jr., 1980, PASP 92, 587
Madore, B.F., Freedman, W.L., 1998, ApJ, 492, 110
Martin, N., Maurice, E., Lequeux, J., 1989, A&A, 215, 219
Martins, F., Schaerer, D., Hillier, D.J., 2002, A&A, 382, 999
Massey, P., Lang, C.C., deGioia-Eastwood, K., Garmany, C.D., 1995,ApJ, 438, 188
Mathewson, D.S., Ford, V.L., Visvanathan, N., 1988, ApJ 333, 617
Mathis, J., 1990, ARA&A, 28, 37
Murai, T., Fujimoto, M., 1980, PASJ, 32, 581
Nelson, C.A., Cook. K.H., Popowski, P., Alves, D.R., 2000, AJ, 119, 1205
Popowski, P., 2000, ApJ, 528, L9
Ribas, I., Guinan, E.F., Fitzpatrick, E.L., DeWarf, L.E., Maloney, F.P., Maurone, P.A., Bradstreet, D.H., Giménez, Á., Pritchard, J.D., 2000, ApJ, 528, 692
Reid, I.N., Strugnell, P.R., 1986, MNRAS, 221, 887
Sasselov, D. D., Beaulieu, J. P., Renault, C., Grison, P., Ferlet, R., Vidal-Madjar, A., Maurice, E., Prevot, L., Aubourg, E., Bareyre, P., Brehin, S., Coutures, C., Delabrouille, N., de Kat, J., Gros, M., Laurent, B., Lachieze-Rey, M., Lesquoy, E., Magneville, C., Milsztajn, A., Moscoso, L., Queinnec, F., Rich, J., Spiro, M., Vigroux, L., Zylberajch, S., Ansari, R., Cavalier, F., Moniez, M., Gry, C., Guibert, J., Moreau, O., Tajhmady, F., 1997, A&A, 324, 471
Schmidt-Kaler, Th., 1982, in Landolt-Börnstein, Group VI, Vol 2b, K. Schaifers & H.H. Voigt (eds), Springer-Verlag
Simon, K.P., Sturm, E., 1994, A&A, 291, 286
Smith, K.C., Howarth, I.D., 1998, MNRAS, 299, 1146
Twarog, B.A., Anthony-Twarog, B.J., Bricker, A.R., 1999, AJ, 117, 1816
Udalski, A., Szymanski, M., Kubiak, M., Pietrzynski, G., Wozniak, P., Zebrun, K., 1998, AcA, 48, 1
Udalski, A., 1998a, AcA., 48, 113
Udalski, A., 1998b, AcA., 48, 383
Udalski, A., Soszynski, I., Szymanski, M., Kubiak, M., Pietrzynski, G., Wozniak, P., Zebrun, K., 1998b, AcA., 48, 563
Underhill, A.B., Divan, L., Prevot-Burnichon, M.L., Doazan, V., 1979, MNRAS, 189, 601
Underhill, A.B., 1982, in B stars with and without emission lines (NASA SP-456)
Vacca, W.D., Garmany, C.D., Shull, J.M., 1996, ApJ, 460, 914
Visvanathan, N., 1985, ApJ, 288, 182
Walborn, N.R., Fitzpatrick, E.L., 1990, PASP, 102, 379
Welch, D., McLaren, R.A., Madore, B.F., McAlary, C.W., 1987, ApJ, 321, 162
Wellstein, S., Langer, N., Braun, H., 2001, A&A, 369, 939
Wegner, W., 1994, MNRAS, 270, 229
Wyithe, J.S.B., Wilson, R.E., 2001, ApJ, 559, 260
Zaritsky, D., Harris, J., Thompson, I.B., Grebel, E.K., Massey, P., 2002, AJ, 123, 855

APPENDIX A

Table 8. Radial-velocity measurements. The first column lists the heliocentric julian date of mid-exposure, while v_p and v_s denote the primary and secondary radial velocities respectively. The errors quoted were determined from the fit covariance matrix.

HJD −240000	v_p (km s^{-1})	v_s (km s^{-1})	v_p (km s^{-1})	v_s (km s^{-1})	v_p (km s^{-1})	v_s (km s^{-1})	v_p (km s^{-1})	v_s (km s^{-1})	v_p (km s^{-1})	v_s (km s^{-1})
	5 038089		**5 202153**		**5 316725**		**6 077224**		**6 158118**	
52158.2834	+412 ± 6	− 3 ± 11	+282 ± 14	0 ± 10	+ 24 ± 12	+436 ± 12			+309 ± 16	− 62 ± 19
52158.9872							+ 33 ± 10	+367 ± 9		
52159.0346							+ 30 ± 11	+380 ± 10		
52159.0641							+ 22 ± 10	+389 ± 10		
52159.1007										
52159.1587							+ 22 ± 11	+373 ± 10	+ 75 ± 13	+402 ± 21
52159.1886			+119 ± 14	+259 ± 11			+ 29 ± 11	+375 ± 9	+ 64 ± 20	+418 ± 23
52159.2430			+ 80 ± 14	+295 ± 3			+ 22 ± 11	+369 ± 10	+ 30 ± 18	+424 ± 10
52160.9686							+335 ± 10	− 23 ± 9		
52161.0089					+ 17 ± 13	+457 ± 10	+358 ± 11	− 16 ± 9		
52161.0992	+414 ± 13	−002 ± 12			+ 18 ± 14	+441 ± 12	+340 ± 11	− 7 ± 10		
52161.1495					+ 28 ± 15	+428 ± 13	+332 ± 11	− 15 ± 10		
52161.1798					+ 40 ± 16	+422 ± 12	+333 ± 11	− 9 ± 10		
52161.2097							+335 ± 11	− 12 ± 10		
52161.2380							+333 ± 11	− 15 ± 10		
52161.2667							+318 ± 11	− 15 ± 10		
52161.2912							+339 ± 11	− 5 ± 10		
52161.9853			+321 ± 7	− 60 ± 10					+ 66 ± 16	+472 ± 22
52162.0273	− 71 ± 14	+421 ± 7	+312 ± 5	− 65 ± 9	+307 ± 16	− 71 ± 13			+ 61 ± 17	+478 ± 21
52162.0714	− 74 ± 14	+415 ± 7	+298 ± 14	− 68 ± 10	+315 ± 12	− 88 ± 13			+ 86 ± 17	+479 ± 21
52162.1128	− 66 ± 13	+416 ± 6	+309 ± 12	− 86 ± 11	+308 ± 16	− 99 ± 13			+ 58 ± 18	+421 ± 15
52162.1506	− 69 ± 15	+411 ± 11	+317 ± 3	− 84 ± 11	+324 ± 10	−114 ± 12			+ 37 ± 18	+430 ± 11
52162.1795	− 67 ± 15	+407 ± 13	+298 ± 14	− 96 ± 11	+316 ± 11	−121 ± 12			+ 71 ± 12	+430 ± 13
52162.2091	− 61 ± 15	+402 ± 13	+314 ± 4	− 79 ± 10	+323 ± 9	−124 ± 12			+ 76 ± 14	+427 ± 9
52162.2375	− 53 ± 15	+395 ± 13	+317 ± 3	− 92 ± 11	+318 ± 8	−120 ± 12			+ 72 ± 12	+414 ± 21
52162.2674	− 48 ± 14	+388 ± 9	+312 ± 6	− 84 ± 11	+318 ± 8	−137 ± 12				
52162.9674			+250 ± 14	+ 17 ± 10			+ 26 ± 11	+369 ± 9		
52163.0101			+270 ± 13	+ 33 ± 10			− 8 ± 10	+381 ± 9		
52163.0531	+415 ± 12	− 6 ± 10	+281 ± 14	+ 61 ± 10			+ 28 ± 11	+382 ± 10	+311 ± 17	− 49 ± 22
52163.0820	+426 ± 12	+ 9 ± 12	+248 ± 14	+ 68 ± 8					+310 ± 17	− 54 ± 22
52163.1104	+428 ± 14	− 16 ± 12	+255 ± 14	+ 73 ± 10			+ 36 ± 11	+377 ± 9		
52163.1405							+ 23 ± 11	+364 ± 10		
	6 215965		**7 243913**		**9 175323**		**11 30116**		**11 57855**	
52158.2834			+356 ± 17	− 67 ± 20						
52158.9872	− 16 ± 12	+358 ± 11			+383 ± 12	− 41 ± 11	+279 ± 14	+ 61 ± 15	+356 ± 14	− 97 ± 15
52159.0346	− 13 ± 11	+375 ± 9					+295 ± 11	+ 29 ± 11		
52159.0641	− 12 ± 11	+384 ± 10							+352 ± 15	−109 ± 18
52159.1007	− 29 ± 12	+361 ± 11								
52159.1587	− 25 ± 11	+381 ± 11					+313 ± 15	− 18 ± 16	+300 ± 7	− 68 ± 19
52159.1886	− 44 ± 12	+375 ± 10								
52159.2430	− 39 ± 12	+373 ± 10	+ 60 ± 17	+425 ± 20			+326 ± 15	− 32 ± 16	+259 ± 14	+ 22 ± 18
52160.9686	+365 ± 9	− 18 ± 10	+343 ± 17	− 56 ± 19	+399 ± 13	− 57 ± 13	+ 65 ± 13	+475 ± 16	− 23 ± 15	+459 ± 20
52161.0089	+321 ± 11	− 34 ± 9								
52161.0992	+360 ± 7	− 37 ± 9								
52161.1495	+367 ± 11	− 47 ± 11			+392 ± 13	− 59 ± 13	+ 70 ± 15	+432 ± 16	+ 43 ± 14	+356 ± 18
52161.1798	+361 ± 7	− 50 ± 10								
52161.2097	+352 ± 12	− 44 ± 11			+379 ± 13	− 31 ± 13	+ 80 ± 15	+414 ± 13		
52161.2380	+355 ± 10	− 54 ± 11								
52161.2667	+366 ± 9	− 55 ± 10								
52161.2912	+369 ± 11	− 37 ± 10								
52161.9853			+ 54 ± 20	+466 ± 20	+ 50 ± 12	+454 ± 8	+287 ± 9	+ 44 ± 16		
52162.0273			+ 48 ± 13	+478 ± 11						
52162.0714			+ 49 ± 15	+479 ± 11	+ 33 ± 11	+478 ± 13	+308 ± 15	+ 2 ± 16		
52162.1128			+ 34 ± 14	+480 ± 11						
52162.1506			+ 45 ± 20	+482 ± 20	+ 17 ± 13	+484 ± 13	+316 ± 15	− 19 ± 16	+ 7 ± 14	+414 ± 6
52162.1795			+ 25 ± 16	+473 ± 10						
52162.2091			+ 41 ± 12	+468 ± 19	+ 20 ± 13	+485 ± 13	+320 ± 15	− 37 ± 15	− 11 ± 11	+447 ± 19
52162.2375			+ 36 ± 18	+464 ± 23						
52162.2674			+ 49 ± 14	+466 ± 17	+ 25 ± 14	+473 ± 14	+328 ± 15	− 51 ± 16	− 17 ± 15	+448 ± 20
52162.9674	− 23 ± 11	+348 ± 11					+292 ± 9	+ 96 ± 16	+366 ± 14	−112 ± 19
52163.0101	− 22 ± 11	+368 ± 10								
52163.0531	− 17 ± 11	+372 ± 11			+380 ± 11	− 1 ± 12			+313 ± 14	− 55 ± 10
52163.0820	− 19 ± 11	+372 ± 10								
52163.1104	− 30 ± 12	+372 ± 11			+395 ± 12	− 22 ± 12			+280 ± 14	− 5 ± 19
52163.1405	− 40 ± 12	+379 ± 9								